Geochemistry, Geophysics, Geosystems®

RESEARCH ARTICLE
10.1029/2021GC010302

# Numerical Modeling of Structurally Controlled Ore Formation in Magmatic-Hydrothermal Systems

**Marta S. Codeço[1,2], Philipp Weis[1,2], and Christine Andersen[1]**

[1]GFZ German Research Centre for Geosciences, Potsdam, Germany, [2]Institute of Earth and Environmental Science, University of Potsdam, Potsdam, Germany

**Key Points:**

- We describe structurally controlled fluid flow by representing faults and fractures as one-dimensional line elements within a 2D modeling domain
- Vertical structures are efficient pathways for focused fluid flow and formation of high-grade mineralization
- Ore formation in horizontal fractures requires a hydraulic connection to distal vertical fault zones

**Supporting Information:**

Supporting Information may be found in the online version of this article.

**Correspondence to:**

M. S. Codeço,
marta.codeco@gfz-potsdam.de

**Citation:**

Codeço, M. S., Weis, P., & Andersen, C. (2022). Numerical modeling of structurally controlled ore formation in magmatic-hydrothermal systems. *Geochemistry, Geophysics, Geosystems*, *23*, e2021GC010302. https://doi.org/10.1029/2021GC010302

Received 14 JAN 2022
Accepted 16 JUL 2022
Corrected 1 SEP 2022

This article was corrected on 1 SEP 2022. See the end of the full text for details.

**Author Contributions:**

**Conceptualization:** Marta S. Codeço, Philipp Weis
**Data curation:** Marta S. Codeço
**Formal analysis:** Marta S. Codeço
**Funding acquisition:** Philipp Weis
**Investigation:** Marta S. Codeço
**Methodology:** Marta S. Codeço, Philipp Weis
**Project Administration:** Philipp Weis



**Abstract** Faults and fractures can be permeable pathways for focused fluid flow in structurally controlled ore-forming hydrothermal systems. However, quantifying their role in fluid flow on the scale of several kilometers with numerical models typically requires high-resolution meshes. This study introduces a modified numerical representation of m-scale fault zones using lower-dimensional elements (here, one-dimensional [1D] elements in a 2D domain) to resolve structurally controlled fluid flow with coarser mesh resolutions and apply the method to magmatic-hydrothermal ore-forming systems. We modeled horizontal and vertical structure-controlled magmatic-hydrothermal deposits to understand the role of permeability and structure connectivity on ore deposition. The simulation results of vertically extended porphyry copper systems show that ore deposition can occur along permeable vertical structures where ascending, overpressured magmatic fluids are cooled by downflowing ambient fluids. Structure permeability and fault location control the distribution of ore grades. In highly permeable structures, the mineralization can span up to 3 km vertically, resulting in heat-pipe mechanisms that promote the ascent of a magmatic vapor phase to an overlying structurally controlled epithermal system. Simulations for the formation of subhorizontal vein-type deposits suggest that the major control on fluid flow and metal deposition along horizontal structures is the absence of vertical structures above the injection location but their presence at greater distances. Using a dynamic permeability model mimicking crack-seal mechanisms within the structures leads to a pulsating behavior of fracture-controlled hydrothermal systems and prevents the inflow of ambient fluids under overpressured conditions.

**Plain Language Summary** Faults and fractures can serve as permeable pathways for focused fluid flow in the subsurface and therefore be essential geological features for the formation of economic mineral deposits. However, quantifying their role in the hydrothermal systems on the scale of several kilometers with numerical models typically requires high-resolution meshes. This study presents a modified numerical representation of m-scale fault zones with variable orientations to understand the hydrology of magmatic-hydrothermal ore-forming systems. The vertically extended systems simulation results show that ore deposition can occur along permeable vertical structures where ascending magmatic fluids are cooled by downflowing ambient fluids. Structure permeability and fault location can directly control the distribution of ore grades. In contrast, mineralization in horizontal structures requires the absence of vertical structures above the injection location of metal-bearing magmatic volatiles but their presence at greater distances. Our model also shows how dynamic opening and closing of the structures in response to magmatic degassing can lead to a pulsating behavior and prevent the downflow of ambient fluids.

## 1. Introduction

The genesis of hydrothermal ore deposits requires favorable geodynamic settings where fluids can transport metals from a large source area through permeable rocks to a locally confined deposition site (Heinrich & Candela, 2014; Kesler & Simon, 2015). However, the bulk permeability of upper crustal rocks generally decreases with depth, and values that permit advective heat and solute transport can be spatially and temporally limited even for tectonically active crust (Ingebritsen & Manning, 1999, 2010). For many major types of hydrothermal ore deposits, active faults and fractures are therefore inferred to serve as high-permeability pathways for focused fluid flow from deeper to shallower depths, including sediment-hosted base metal, orogenic gold, unconformity-related uranium, submarine massive sulfide, polymetallic vein-type and epithermal precious metal deposits (Cox, 2005; Heinrich & Candela, 2014). Fluid overpressure can further increase permeability by hydraulic fracturing, eventually resulting in the formation of mineralized hydrothermal veins, stockworks, and breccias (Cox, 2005; Heinrich & Candela, 2014).

**Software:** Marta S. Codeço, Philipp Weis
**Supervision:** Philipp Weis
**Validation:** Marta S. Codeço, Philipp Weis
**Writing – original draft:** Marta S. Codeço
**Writing – review & editing:** Marta S. Codeço, Philipp Weis, Christine Andersen

In magmatic-hydrothermal ore-forming systems, fluid overpressures are caused by hydrous magmas intruded into the upper crust, which release magmatic volatiles during cooling and crystallization. In the absence of pre-existing structures, fluid release can lead to multiple fracturing events of the overlying host rocks, increasing the bulk permeability and creating stockwork veining, most prominently observed in porphyry-copper systems (Sillitoe, 2010). Some porphyry deposits also show a structural control of the mineralization, such as the giant Chuquicamata deposit in Chile, where the mineralization has a vertical extent of up to 3 km along a fault zone (Ossandon et al., 2001). However, it is unclear to which degree the current outline of the ore shell at Chuquicamata has been affected by supergene enrichment and later fault displacement, which could mean that the currently mined deposit is only one part of the original hypogene mineralization (Pinget, 2016; Pinget M. et al., 2015; Zentilli et al., 2021).

Epithermal Au-Ag-Cu deposits can form at further distances from the intrusion and shallower crustal levels (Hedenquist & Lowenstern, 1994). They typically show a structural control with mineralized veins forming due to focused fluid flow along permeable fault or fracture zones. Such a structural control combined with stratabound mineralization can also be observed at the world-class Carlin-type Au deposits in Nevada, USA. Their formation process is debated, with many observations pointing toward a magmatic-hydrothermal origin (Muntean et al., 2011).

Structurally controlled fluid flow in initially low-permeability host rocks has also been interpreted as a key for the generation of magmatic-hydrothermal deposits associated with compressional and/or transpressional (post-)orogenic settings and highly evolved Sn-W granites (Foxford et al., 2000; Jacques et al., 2018; Polya et al., 2000; Černý et al., 2005). A prominent example is the Panasqueira W-Sn-Cu vein-type deposit in Portugal, which consists of mineralized sub-horizontal veins nearby a Variscan granitic intrusion that formed from focused flow of magmatic fluids with variable degrees of fluid mixing during later stages (Kelly & Rye, 1979; Polya et al., 2000). Structural studies indicate that fluid flow during the expulsion of magmatic volatiles uses pre-existing horizontal structures that have been initiated during transpressional tectonics pre-dating the magmatic-hydrothermal ore-forming event (Jacques et al., 2018). On the other hand, field observations also indicate the presence and influence of steeply dipping fault zones in the deposit, which may have been reactivated sometime during ore formation (Polya, 1988). Sub-horizontally oriented vein structures have also been described in other magmatic-hydrothermal ore deposits, such as the Zinnwald Sn-W-Li deposit, and in the root zones of some porphyry Cu deposits (Runyon et al., 2017; Webster et al., 2004).

Numerical simulations with models that can handle high-temperature multiphase flow of NaCl-$H_2O$ fluids in porous media can help quantify the dynamic behavior of mass and heat transfer in magma-related hydrothermal systems (Ingebritsen et al., 2010). Previous studies focused on the physical hydrology of porphyry and epithermal deposits (Blundy et al., 2021; Weis et al., 2012) and active hydrothermal systems (Andersen et al., 2015; Coumou et al., 2008; Gruen et al., 2014; Hasenclever et al., 2014; Kissling et al., 2015). In these models, permeability values are typically used as bulk parameters, and where high-permeability fault zones have been considered, they are resolved by fine mesh sizes, which is computationally expensive.

As an alternative approach, previous simulations using the Complex Systems Modeling Platform CSMP++ calculated fluid flow in fracture networks within domains with dimensions of several meters by introducing lower-dimensional elements (i.e., representing structures as 1D line elements in a 2D domain or 2D elements in a 3D domain) to represent fracture apertures as local permeability increases (Geiger & Emmanuel, 2010; Matthäi & Belayneh, 2004). This approach can resolve networks of discrete fractures within modeling domains on the m-scale with apertures below 1 cm. Hence, resolving fluid flow on the scale of several kilometers with an identical approach would still lead to very fine mesh sizes. Instead, modeling structurally controlled fluid flow on the km scale requires the resolution of fault zones and oriented fracture networks on the m-scale. For this study, we therefore developed a modified approach for the use of mixed-dimensional elements (here, 1D line elements within a 2D domain) to describe locally increased permeability values due to fracturing around geological structures with either user-defined values for fault width and permeability, or dynamic permeability evolution due to hydraulic fracturing.

We present results from numerical simulations of the hydrology of structurally controlled magmatic-hydrothermal ore systems, using generic model geometries with schematic representations of key geological structures with variable orientations. These structures are taken from geological observations at the world-class deposits

Chuquicamata and Panasqueira. However, full reconstructions of the formation of individual deposits are beyond the scope of this study because they are often the result of a complex superposition of several events. Thus, our numerical simulations rather aim to investigate the role of sub-vertically and sub-horizontally oriented structures and different scenarios of dynamic permeability evolution.

## 2. Methods

### 2.1. Governing Equations

Conservation of mass, energy, and momentum are the principal laws that describe fluid flow in hydrothermal systems (Ingebritsen et al., 2006). We solve for the governing equations with a Control Volume Finite Element method (CVFEM) implemented into the Complex Systems Modeling Platform (CSMP++), which can describe compressible flow of variably miscible, multiphase fluids (Weis et al., 2014). The properties of saline fluids are calculated using the NaCl-$H_2O$ system as described by Driesner and Heinrich (2007) and Driesner (2007).

Two-phase fluid flow in fractured and porous media can be described by Darcy's law as

$$v_i = -k\frac{k_{ri}}{\mu_i}\left(\nabla p - \rho_i g\right),\ i = l,\ v \tag{1}$$

where $v$ is the Darcy velocity of the mobile phases $i$ (liquid $l$ and vapor $v$), $k$ is the permeability, $k_r$ is the relative permeability, $\mu$ is viscosity, $p$ is pressure, $\rho$ is density, and $g$ is the acceleration due to gravity in the vertical direction. Solid halite $h$ is assumed to reduce the available permeability and block pore space. For the mobile phases, a linear relative permeability model is applied, ensuring that $k_{rv} + k_{rl} = 1-S_h$, with $S$ as the volumetric saturation of the indicated phase. The residual saturation $R_l$ has been set to $0.3(1-S_h)$ for the liquid phase and 0.0 for the vapor phase (Weis et al., 2014).

The conservation of total fluid mass, salt mass, and energy are given by the following expressions, respectively:

$$\frac{\partial\left(\phi\left(S_l\rho_l + S_v\rho_v + S_h\rho_h\right)\right)}{\partial t} = -\nabla\left(v_l\rho_l\right) - \nabla\left(v_v\rho_v\right) + Q_{\mathrm{H_2O+NaCl}} \tag{2}$$

$$\frac{\partial\left(\phi\left(S_l\rho_l X_l + S_v\rho_v X_v + S_h\rho_h\right)\right)}{\partial t} = -\nabla\left(v_l\rho_l X_l\right) - \nabla\left(v_v\rho_v X_v\right) + Q_{\mathrm{NaCl}} \tag{3}$$

$$\frac{\partial\left((1-\phi)\left(\rho_r h_r + \phi(S_l\rho_l h_l + S_v\rho_v h_v + S_h\rho_h h_h)\right)\right)}{\partial t} = \nabla(K\nabla T) - \nabla\left(v_l\rho_l h_l\right) - \nabla\left(v_v\rho_v h_v\right) + Q_e \tag{4}$$

where $\phi$ is the porosity, $h$ the specific enthalpy, $X$ the mass fraction of NaCl in the respective phase, $t$ the time, $K$ the thermal conductivity, $T$ the temperature and $Q_{\mathrm{H_2O+NaCl}}$, $Q_{\mathrm{NaCl}}$, and $Q_e$ are source terms. The subscript $r$ stands for the rock matrix. In this approach, we assume that fluid and rock are in local thermal equilibrium, requiring that the total enthalpy is distributed over the fluid and rock contained in a control volume (Weis et al., 2014).

For this study, we use meshes consisting of 2D triangular finite elements (green outline in Figure 1a). The node-centered control volumes are then defined by facets (blue lines) which connect the finite element's face mid-points with the element's barycenter. By introducing lower-dimensional (1D) elements representing the fault zones into the 2D mesh (red line in Figure 1b), we are creating additional fault-related facets (orange line), which are perpendicular to the orientation of the element and located at the mid-point between the two neighboring nodes.

Fluid advection is calculated across facets within finite elements and between neighboring node-centered control volumes with the background permeability $k_b$ of the given element, representing the rock matrix. In the integral form of Darcy's Law, the total discharge $Q_{\mathrm{AB}_i} = Av_i$ through the cross-sectional area $A$ for fluid phase $i$ between nodes A and B (gray arrows in 1a) can be formulated using the facets $f_1$ and $f_2$ from the triangular finite elements $e_1$ and $e_2$, respectively as:

$$Q_{AB_i} = l_{f_1}k_b\left(\frac{k_{ri}}{\mu_i}\right)_u\left(\nabla p_{e_1} - \rho_{iu}\vec{g}\right)\cdot\overrightarrow{n_{f_1}} + l_{f_2}k_b\left(\frac{k_{ri}}{\mu_i}\right)_u\left(\nabla p_{e_2} - \rho_{iu}\vec{g}\right)\cdot\overrightarrow{n_{f_2}} \tag{5}$$

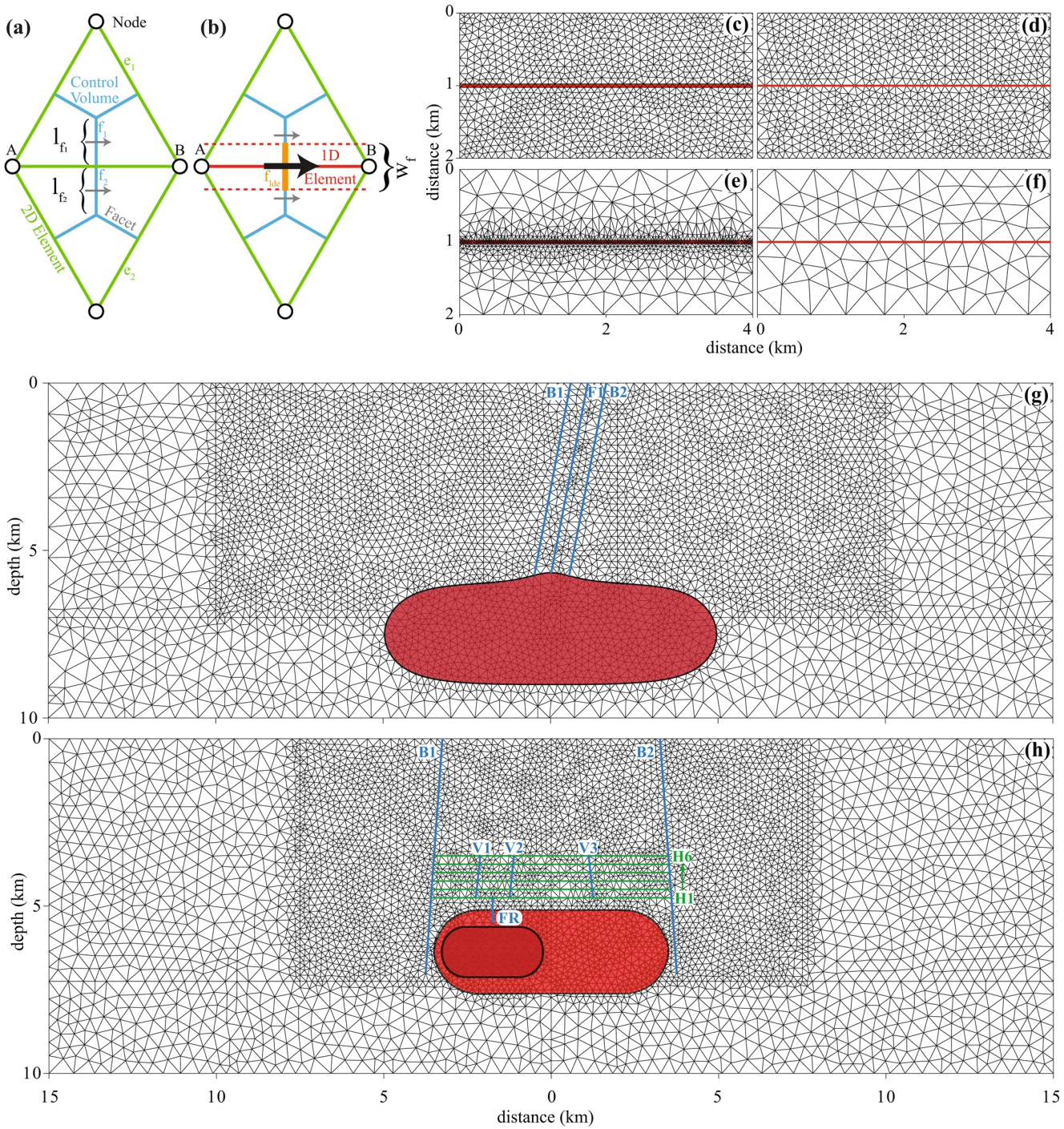


**Figure 1.** Mesh geometries using mixed-dimensional elements for simulations of structurally controlled hydrothermal systems (a, b) Representation of fracture flow within a two-dimensional (2D) mesh of triangular finite elements (green) with lower-dimensional (1D) line elements (red) and superimposed node-centered control volumes (blue). (a) Fluid flow (gray arrows) between two neighboring nodes (A and B) is calculated across the facets ($f_1$ and $f_2$) of the 2D elements ($e_1$ and $e_2$), with $l_{f_1}$ and $l_{f_2}$representing the facet length. (b) The additional flux through higher-permeability faults and fractures (black arrow) is calculated across the facet of the 1D (lower-dimensional) element ($f_{1de}$) (orange) with a user-defined width ($w_f$) (dashed red lines). See Text S1 in Supporting Information S1 for further details (c–f) Mesh geometries of a two-dimensional modeling domain (2 × 4 km) with a fault zone of 50 m width resolved by triangular elements (red band in c and e) or line elements (red line in d and f) using fine (c, d) and coarse (e, f) resolutions of the host rock (g, h) Domains of 10 × 30 km representing a cross-section of the upper crust for porphyry copper (g) and vein-type (h) systems, including a magmatic body (red) 5 km depth with a partially molten reservoir (dark red), vertical fault zones (blue; vertical faults F1, F2, and F3, fluid release structure FR, and bounding faults B1 and B2) and horizontal fracture zones (green).

with the index $u$ for the upstream values of fluid properties, the facet normal $\vec{n}$ and the facet length $l_f$. For 2D simulations, the unresolved third dimension has a nominal thickness of 1 m. Hence, $l_f$ represents a cross-sectional area in $m^2$ and $Q$ has units of $m^3/s$. A detailed description of the CVFEM implementations is provided in Weis et al. (2014).

In 2D simulations, the additional influence of fault permeability of each 1D line element can be described by the difference between the fault/fracture permeability $k_f$ and the background permeability $k_b$, and the width $w_f$ of the fault or fracture zone (distance between dashed red lines in Figure 1). We introduce an additional term to the total discharge that considers the influence of the additional flow (black arrow) across the facet of the lower-dimensional element ($f_{lde}$):

$$Q^*_{\mathrm{AB}_i} = Q_{\mathrm{AB}_i} + w_f\,(k_f - k_b)\left(\frac{k_{ri}}{\mu_i}\right)_u \left(\nabla p_{lde} - \rho_{iu}\vec{g}\right)\cdot\overrightarrow{n_{f_{lde}}} \tag{6}$$

Again, considering the nominal thickness for 2D simulations, $w_f$ represents a cross-sectional area in $m^2$. This formulation is valid for $k_f \geq k_b$ and $w_f/2 \leq l_f$. The influence of the respective fault segment vanishes when the fault has the same permeability as the rock matrix ($k_f = k_b$) or if $w_f = 0$.

### 2.2. Simple Fault Zone

We first use a horizontal model domain of $2 \times 4$ km with a background permeability of $k_b = 10^{-15}$ $m^2$ and a fault zone with a width of $w_f = 50$ m and permeability of $k_f = 10^{-14}$ $m^2$ in the center of the domain (Figures 1c and 1d). With a uniform resolution using element sizes similar to $w_f$, the fault structure can either be resolved by one line of 2D triangles within the normal 2D approach (Figure 1c; 1,930-triangular elements) or one line of 1D elements within the mixed-dimensional method (Figure 1d; 1,657-triangular and 36-line elements). In the latter mesh, the width of the superimposed 1D element representing the fault zone will roughly coincide with the barycenter of the 2D triangle elements of the host rock, which is the limit of validity for the approach (Figure 1b). With a much coarser resolution of the host rock but a higher resolution within the fault zone, the all-triangle mesh needs to be gradually refined toward the high-resolution center part (Figure 1e; 1,710 triangular elements). Using the same coarse resolution for the host rock in the mixed-dimensional element approach results in a significant reduction in the number of triangular elements representing the same geological setting (Figure 1f; 173-triangular and 13-line elements).

Our fluid flow simulations along this simple fault zone serve as verification for the new formulation. We prescribe a temperature and pressure decrease from left to right by applying constant boundary conditions with $T_{\mathrm{left}} = 350$°C, $p_{\mathrm{left}} = 35$ MPa, $T_{\mathrm{right}} = 150$°C, and $p_{\mathrm{right}} = 25$ MPa (Weis et al., 2014). We use a constant porosity of 10%, thermal conductivity of 2 W $m^{-1}$°$C^{-1}$, and heat capacity of 880 J $kg^{-1}$°$C^{-1}$. The domain is initialized with the temperature conditions of the right boundary, leading to the transient evolution of a temperature front from left to right during the simulation.

### 2.3. Magmatic-Hydrothermal Systems

#### 2.3.1. Dynamic Permeability and Proxies

For the simulations of magmatic-hydrothermal systems, we further apply a model for dynamic permeability evolution (Weis et al., 2012) that describes permeability decrease at temperatures above the brittle-ductile transition and permeability increase due to hydraulic fracturing at fluid pressures above a temperature-dependent failure criterion (see detailed description in Weis, 2015). For the present study, we have also adapted this model for permeability variations in pre-existing geologic structures defined in the respective modeling domain.

The dynamic permeability model uses an ad-hoc parameterization with incremental permeability increase once fluid pressure ($p_{\mathrm{fluid}}$) locally reaches a calculated failure criterion ($p_{\mathrm{failure}}$). For the newly implemented functionality for structure permeability, we incrementally increase $k_f$. However, we impose maximum permeability values for this incremental opening to assure geologically realistic values (for example, $10^{-14}$ or $10^{-13}$ $m^2$ (Agheshlui et al., 2018; Mavko et al., 2009)). We ensure that $p_{\mathrm{fluid}} \leq p_{\mathrm{failure}}$ by converting any further increase in fluid pressure into an additional porosity $\Delta\phi$ (reflecting dilation and/or increase in fracture apertures) that is needed

for the compressible fluids to maintain $p_{\text{fluid}} = p_{\text{failure}}$ during hydraulic fracturing (adapted from Equation 13 in Lamy-Chappuis et al. (2020)).

$$\Delta\phi(overpressure) = \phi\left(\frac{\rho_m}{\rho_f\left(X_{\text{NaCl}}, T, p_{\text{failure}}\right)} - 1\right) \tag{7}$$

where $\rho_f$ is the thermodynamic density at $p_{\text{fluid}} = p_{\text{failure}}$ and $\rho_m = \frac{m_l + m_v + m_h}{\phi V}$ is the total fluid mass per pore volume (see Weis et al., 2014 for details of the numerical implementation of the CVFEM scheme). However, this excess volume is considered to be reversible and is still used for calculating fluid flow because otherwise, the driving force would vanish in horizontal structures (i.e., no horizontal pressure gradient for $p_{\text{fluid}} = p_{\text{failure}}$ and no buoyancy force in Equation 1).

The simulations focus on the evolution of the physical hydrology in such a transient, anisotropic, heterogeneous permeability field. We further derive simplified proxies to constrain their ore-forming potentials. For the vertically extended porphyry-like setup, we assume that the magmatic fluids precipitate their copper content during cooling within the temperature interval between 450°C and 350°C and calculate a copper enrichment potential as the ratio between precipitated copper and initial copper content (for details, see Weis, 2015). For the subhorizontal vein-type setup, we assume that fluid-rock interactions are of critical importance and monitor the integrated mass flux of magmatic fluids through a respective volume of rock over the entire simulation period.

#### 2.3.2. Geometries and Meshes

For the simulations of structurally controlled mineralization in magmatic-hydrothermal systems, we use two vertical cross-sections of the upper crust of 10 × 30 km with magmatic intrusions at 5 km depth with vertical (blue and red line elements) and mixed vertical (green elements) and horizontal (blue elements) structures (Figures 1g and 1h, respectively). The mixed-dimensional approach enables using relatively coarse meshes while still resolving the influence of faults and fractures (Figure 1g: 9,533-triangular and 122-line elements; h: 10,614-triangular and 450-line elements). The geometries are still generic but use dimensions and orientations of the structures from conceptual models of well-studied deposits. With the first geometry, we investigate the influence of active fault zones during the formation of porphyry deposits (Figure 1g; conceptualized from the Chuquicamata deposit). With the second geometry, we investigate the relative influence of horizontal and vertical fault zones and fracture networks on subhorizontal vein-type deposits (Figure 1h, conceptualized from the Panasqueira deposit).

In magmatic-hydrothermal deposits, field observations and numerical modeling show that fluid release from magmatic bodies can be focused through a cupola region (e.g., Burnham, 1979; Dilles, 1987; Richards, 2021; Shinohara & Hedenquist, 1997). Fluids are released directly into the host rocks in the porphyry-like setup and into a permeable structure in the horizontal vein-type deposit setup.

At Chuquicamata (Figure 1g), the West fault system controls the intrusions, mineralization, and post-mineralization processes (Ossandon et al., 2001). The geometry (Figure 1g) used in this study is based on the 3600N section (Ossandon et al., 2001; Figure 6) and further structural information (Skarmeta, 2021). The vein systems were formed during early movements between the Massabi Fault (here represented by B2, Figure 1g) in the East and the West fault system (B1 in Figure 1g). According to Skarmeta (2021), fault-vein relationships showing mutual crosscutting and common alteration-mineral infill suggest an intimate and synchronous development. Moreover, vertical fracturing and hydraulic fluid discharge may have caused late veining and brecciation within the Americana Fault (F1: Figure 1g) (Faunes et al., 2005; Fournier, 1999; Ossandon et al., 2001).

Geophysical data and geological observations indicate that the Panasqueira Granite is bounded by two major faults (Ribeiro, 2017) schematically included in our geometry as bounding fault zones B1 and B2. We also consider that the mineralization is asymmetrically located at the Northwestern part of the granite, that is, in the geometry to the left side of the assumed injection point at the cupola. The set of horizontal structures (H1–H6) schematically represents swarms of many subhorizontal veins with variable widths. When activated, these structures introduce a fracture-dominated anisotropy of the regional permeability field rather than representing single fractures/veins, which would require very fine mesh resolutions. Several field-related studies further infer that pre-existing vertical fault structures in the host rock above the intrusion have been reactivated and used as permeable pathways for fluid flow during ore formation (Thadeu, 1951). In an assumed compressional stress regime during ore formation, which would favor the formation of horizontal structures, these steeply-dipping

faults would be severely misoriented. However, previous studies have suggested that these pre-existing structures can still be activated during hydraulic fracturing (Cox et al., 2001; Sibson, 1996). Other structural models infer different mechanisms for vertical pathways to explain the connectivity between the subhorizontal levels. Our modeling study cannot resolve the structural geology of the deposit, but we schematically include three vertical structures as V1, V2, and V3, which can be activated or deactivated in different modeling setups.

#### 2.3.3. Model Configuration and Assumptions

We further vary the properties of the magma chamber, host rock, and structures according to their different geological characteristics. An initial 900°C hot volume of magma with a solidus temperature of 700°C is used in the porphyry-like model, reflecting a typical hydrous andesitic source magma (Weis et al., 2012). To account for the release of latent heat of crystallization, we take an initially doubled heat capacity for the intrusion, which is gradually decreased upon cooling (Hayba & Ingebritsen, 1997). Fluid release considers focusing from an assumed third dimension into the 2D-cross-section of the model domain as adapted from and described in detail for numerical simulations of porphyry copper systems (Weis, 2015), resulting in a 3D-reservoir with dimensions of ~10 (×5) × 3 km (assuming a factor of 0.5 for the lateral extent into the third dimension). We assume an initial fluid salinity of 10 wt.% NaCl and copper content of 500 ppm, which are modeled to be released to the host rock in proportion to the cooling and crystallization rate through the uppermost part of the intrusion.

For the subhorizontal vein-type deposit setup, we assume an evolved, hydrous granitic magma with a solidus temperature of 650°C (Pichavant & Manning, 1984), where the dimensions of the larger magma body [7 (×3.5) × 2.5 km] have been taken from geophysical data (Ribeiro, 2017). However, we start the simulation of an ore-forming event at a time when most of the magma body has already reached the solidus temperature (light red: initial temperature of 650°C; Figure 1h), while only a subdomain is still hotter (dark red: initial temperature of 750°C) and releases fluids with an initial salinity of 5 wt.% NaCl (Bussink, 1984; Kelly & Rye, 1979; Lecumberri-Sanchez et al., 2017) during cooling. This volume reflects the fraction of the reservoir (including the inferred third dimension) needed to produce the amount of magmatic fluids (1.5 Gt) required to provide a total of 150,000 t of W for the Panasqueira deposit (Polya, 1988), assuming a water content of 5% for the magma and fluid concentrations of 100 ppm W. The latter value is inferred from reconstructed fluid concentrations calculated from white mica compositions at Panasqueira (~40 ppm W; Codeço et al., 2021) and fluid inclusion analyses from the Zinnwald Sn-W deposit (average 100 ppm W; Korges et al., 2018). However, fluid inclusions from Panasqueira indicate lower W contents (6 ppm, Lecumberri-Sanchez et al., 2017), and other estimates may infer larger amounts of total W for the deposit, which would require either a larger subdomain or higher water contents of the magma. Hence, our simulations likely reflect a minimum estimate for magmatic fluid release.

In the porphyry-like setup, we assume a depth-dependent background permeability profile with a value of $10^{-14}$ $m^2$ for the uppermost 1 km (Ingebritsen & Manning, 2010), whereas, in the vein-type model, we assume that the metasedimentary host rock has a relatively low permeability with $10^{-16}$ $m^2$ for the uppermost 1 km and a depth-dependent decrease below that. This function is superimposed by a temperature-dependent permeability decrease representing the brittle-ductile transition, starting at 360°C for the silica-rich igneous host rocks typical for porphyry environments and 650°C for the relatively silica-poor host rock in the vein-type example (Fournier, 1999; Hayba & Ingebritsen, 1997).

In all simulations, the top boundary represents the subaerial paleo-surface by using constant atmospheric pressure conditions for the model. Fluids can leave through the surface at temperatures calculated by the model, and recharging fluids have a temperature of 20°C. We apply no-flow boundaries at the sides, and a constant heat flux of 45 mW $m^{-2}$ at the bottom boundary maintains a background geothermal gradient of 22.5°C $km^{-1}$, which is also applied as initial conditions for the domain surrounding the magmatic intrusion.

This study presents a set of simulations for the porphyry-like and subhorizontal vein-type setups by varying parameters such as permeability, structure location, and connectivity. These types of magmatic-hydrothermal deposits can be transitional in the physical behavior during formation, but we use two end-member scenarios to investigate two different kinds of dynamic permeability evolution:

1. For the vertically extended porphyry system setup, we use the dynamic permeability model for the host rock (i.e., as a dynamic bulk property of 2D triangular elements), reflecting multiple events of small vein formation in porphyry stockworks, but with constant, elevated permeability values for pre-existing fault zones represented by 1D line elements. This model parameterization assumes a near-critically stressed host rock for

brittle conditions, leading to failure at fluid pressures above hydrostatic values. Differential stress is reduced with increasingly ductile behavior, leading to failure at near-lithostatic fluid pressures.

2. For the subhorizontal magmatic-hydrothermal vein-type deposit setup, we reverse this configuration by keeping the low-permeability profile of the host rock and modeling dynamic hydraulic fracturing for the pre-existing structures only (i.e., as dynamic permeability evolution along the orientation of the 1D line elements), reflecting crack-seal cycles during vein formation of discrete fractures and fault structures. In this model parameterization, we assume that fluid pressures have to reach supralithostatic values for hydraulic fracturing and permeability increase.

## 3. Results

### 3.1. Fluid Flow Along a Simple Fault Zone

Fluid flow along a high-permeability fault zone leads to faster propagation of the thermal front compared to flow through the lower-permeability host rock (Figure 2). After 2,000 years of simulation time, the 200°C isotherm has approximately reached the right boundary within the fault zone and the middle of the domain in the host rock at the top and bottom boundaries. The areas of the host rock immediately surrounding the fault zone are mainly heated by conduction, resulting in a widening of the thermal front upstream. Using similar mesh resolutions

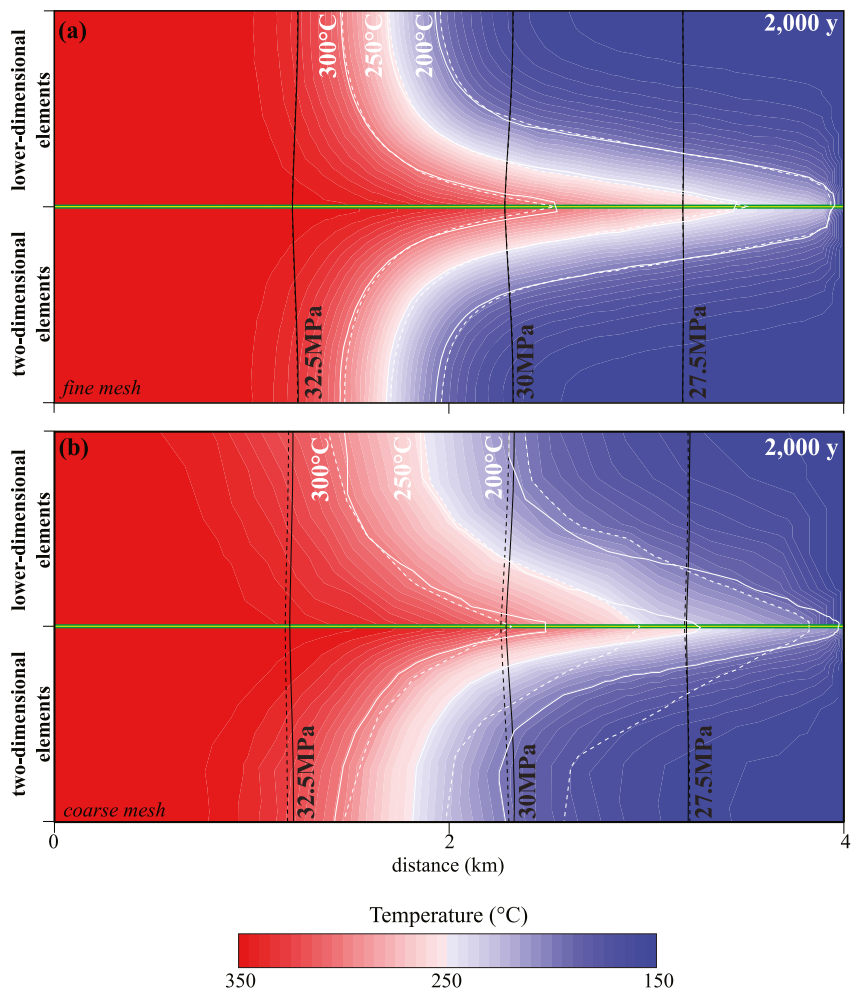


**Figure 2.** Snapshots after 2,000 years of the propagation of a thermal front along a fault structure that is either resolved by two-dimensional (lower half) or one-dimensional (upper half) elements on meshes with fine (a) and coarse (b) resolution. Results for fluid pressure (black) and temperature (white) from lower-dimensional simulations are plotted as dashed lines, and results from two-dimensional simulations as solid lines. The yellow line represents the lower-dimensional fracture, and the green band represents the 50 m-wide fault zone.

results in almost identical results for the new mixed-dimensional approach (Figure 2a, upper half) and the conventional all-triangles approach (Figure 2a, lower half), confirming that the newly implemented functionality can adequately capture structurally controlled fluid flow.

Decreasing the resolution of the host rock leads to a smoother thermal front (Figure 2b). While the 300°C isotherm is at the same location as in Figure 2a, the 200°C isotherm has already progressed a few hundred meters further. Increasing the resolution within the fault zone in the all-triangles approach decreases the area of the host rock that is heated in the vicinity of the fault zone by conduction, resulting in a narrower front (Figure 2b, lower part). In contrast, the simulation with the coarse mixed-dimensional mesh results in a wider thermal front with propagation slightly overestimated in the host rock and underestimated in the fault zone. The latter is an effect of the assumed local thermal equilibrium in the respective control volumes because the incoming hotter fluid has to heat up a larger volume of rock. Fluid pressures are only weakly affected by varying the mesh type.

Despite these mesh-dependent differences, the four simulations roughly agree on the positions and shapes of the thermal fronts. Hence, both approaches and different mesh resolutions can adequately capture the first-order flow patterns. While the higher-resolution meshes will naturally produce the most accurate solutions, the results show that the representation of fault structures by lower-dimensional elements enables the use of coarse-resolution meshes in order to save computational time and still capture structurally controlled fluid dynamics.

### 3.2. Vertically Extended Porphyry Systems

#### 3.2.1. Evolution of the Physical Hydrology With Fault Control

In our simulations of porphyry systems, the intrusion is gradually cooled by conductively heating the adjacent host rock and convecting ambient fluids. Magmatic fluids are released at the uppermost part of the magma chamber as soon as the outer rim reaches the solidus temperature (700°C) (Figure 3a). Fluid expulsion leads to increased fluid pressures above the intrusion with maximum pressures above the injection location, where the permeability is initially lowered due to increasingly ductile behavior at high temperatures (Figure 3b). However, the permeability of the nominally ductile crust (where the dynamic permeability model assumes that differential stresses are reduced) can be temporarily increased due to hydraulic fracturing once fluid pressures reach failure at near-lithostatic values, resulting in the opening of additional porosity (up to 0.1%) (Figure 3b). At lower temperatures, the critically stressed brittle crust rapidly reaches the failure criterion at near-hydrostatic pressures, resulting in a broader stimulated area due to far-field pressurization. During ascent, the fluids are preferably focused in the two permeable fault zones (Figure 3c).

After 5,000 years, magmatic fluids dominate in the area above the cupola (Figure 3d), and overpressured permeability/porosity waves ascend through the host rock from the cupola toward the surface (Figure 3e). At shallower levels (~2 km), mixing with colder meteoric waters leads to a sudden drop in temperature (500°C–200°C) and pressure (75–~20 MPa) (Figures 3d and 3e). The fluids are injected in a single-phase state and phase separate into a low-salinity, low-density vapor, and high-salinity, high-density brine upon ascent. The vapor phase ascends toward the surface at higher velocities than the brine phase (Figure 3f), leading to an increase in bulk fluid salinities of >30% wt.% NaCl (Figure 3e). Under near-lithostatic fluid pressure gradients in the central upflow zone, dense brine can still move upwards. Due to the higher constant permeability values, fluids within the fault zones have near-hydrostatic fluid pressures and are characterized by two-phase conditions. Here, the higher-density, lower-enthalpy brine phase moves downward, while the lower-density, higher-enthalpy vapor phase moves upward, forming a so-called heat pipe which is an efficient mechanism for heat transfer from depth to the surface. During this stage, the magmatic vapor phase is transported to shallower levels along both vertical structures, where it also mixes with meteoric fluids (Figure 3f).

During the waning stage after 30,000 years, the magma chamber has cooled significantly from the initial temperature. However, the hydrothermal system above the injection zone prevents the roof of the magma chamber from being cooled. As the magma chamber cools from the sides, the surface area decreases, leading to a lower fluid production rate. Consequently, the incursion of meteoric waters efficiently cools the magmatic front, resulting in its retreat to deeper levels (3–4 km).

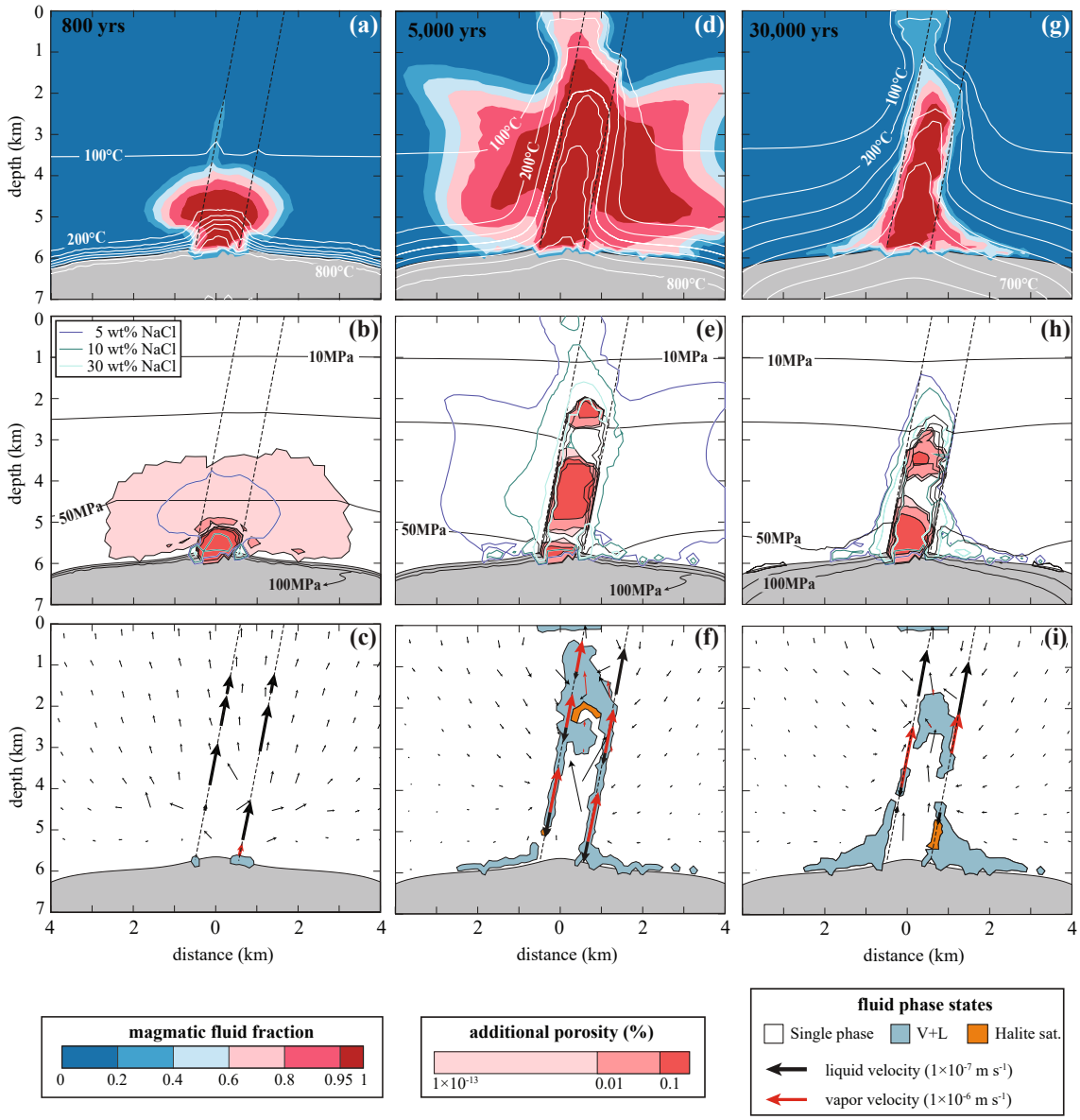


**Figure 3.** Temporal and spatial evolution of a magmatic-hydrothermal system with structurally controlled fluid flow along two subvertical bounding faults ($w_f$ (B1) = 50 m, $w_f$ (B2) = 20 m and $k_f = 10^{-14}$ m$^2$) after 800 years (a, b, c), 5,000 years (d, e, f) and 30,000 years (g, h, i), showing: (a, d, g) the fraction of magmatic fluids and the temperature (white lines); (b, e, h) additional porosity, bulk salinity and fluid pressure (black lines) as well as (g, h, i) fluid phase states and liquid (*L*) and vapor (*V*) velocities (only a selection of arrows with different scaling factors are shown for graphical reasons).

### 3.2.2. Variations in Fault Control

With an increased permeability value for the left (B1) fault ($10^{-13}$ m$^2$), the fluids can be more readily transported toward the surface by the ascending magmatic vapor phase (Figures 4a–4c). Due to the higher permeability contrast, fluid pressures within the fault zone dramatically decrease to values well below the hydrostatic pressure values of the colder regions in the neighboring host rock, ensuring the inflow of convecting meteoric fluids from the area left of the fault (Figure 4b). This change leads to higher liquid velocities for the downward flow compared to the previous simulation (Figure 3f) and a stronger influence of meteoric fluids within the fault zone. The larger amount of admixing meteoric fluids leads to stronger cooling, and fluid mixing already starts at deeper levels. The left (B1) fault now acts as a hydrological divide with complete absence of any magmatic fluids in the areas to the left of it, except for the uppermost km, where there is only one order of permeability contrast between host rock and fault zone ($k_f = 10^{-13}$ m$^2$, $k_b = 10^{-14}$ m$^2$).

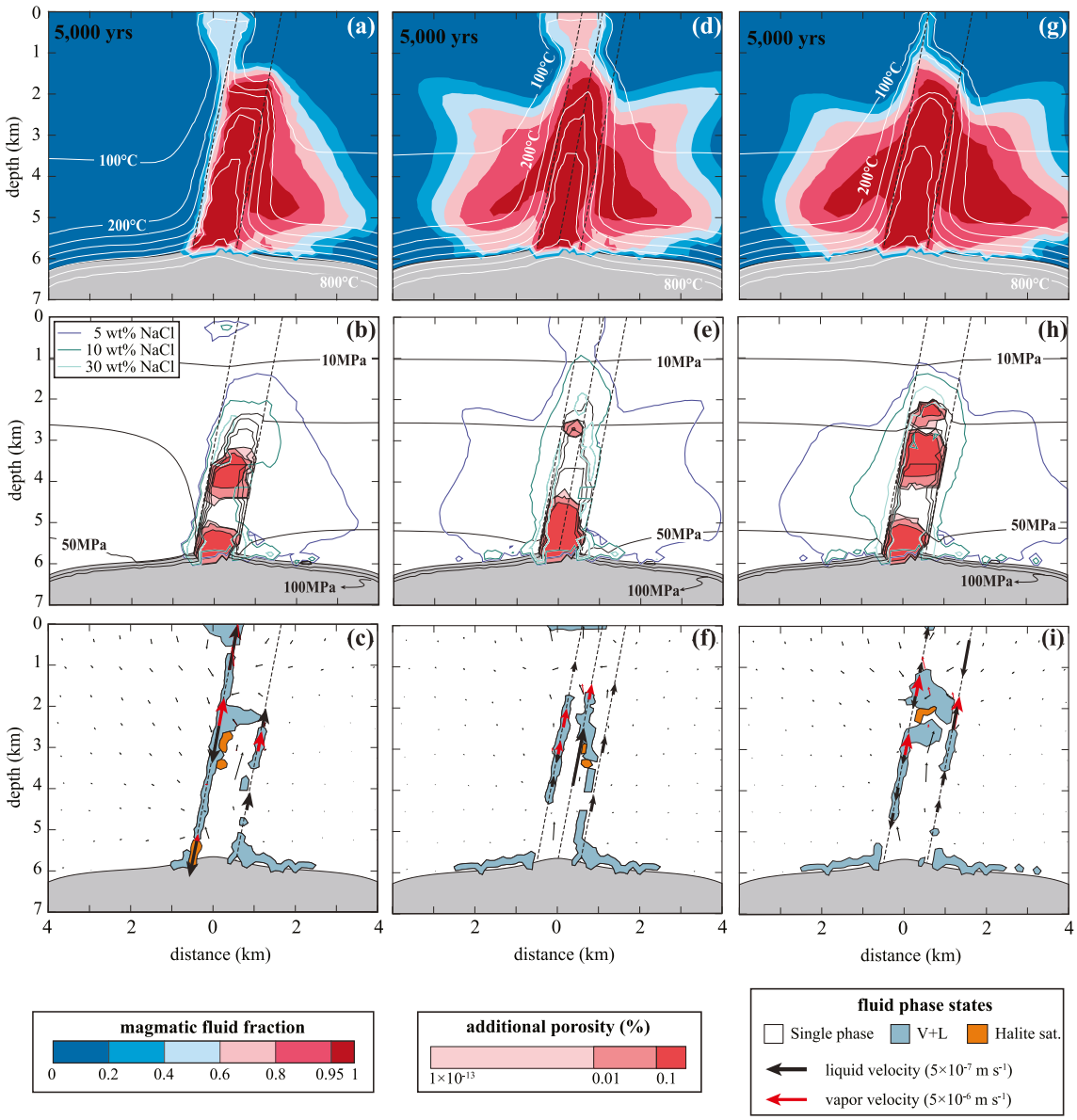


**Figure 4.** The influence of fault permeabilities and arrangements on the hydrothermal system with a higher permeability in the left fault zone ($k_f$ (B1) = $10^{-13}$ m$^2$; (a, b, c), an additional central fault zone ($w_f$ (F1) = 10 m, $k_f$ (F1) = $10^{-14}$ m$^2$; (d, e, f) and higher fault permeabilities in the uppermost parts of the fault zones ($k_f$ (0–1 km depth) = $10^{-12}$ m$^2$; g, h, i) (a, d, g) Fraction of magmatic fluids and the temperature (white lines); (b, e, h) additional porosity, bulk salinity, and fluid pressure (black lines) as well as (g, h, i) fluid phase states and liquid (*L*) and vapor (*V*) velocities during the peak of the magmatic-hydrothermal system (at 5,000 years).

Adding a third central structure (F1) to the original scenario and using the same permeability for all three fault zones ($10^{-14}$ m$^2$) results in a similar evolution of the magmatic and thermal fronts (Figure 4d). However, the fluid pressure develops a much narrower profile (Figure 4e) due to a greater focusing of fluids through the central fault, where fluid velocities are more than three orders of magnitude higher than in the right (B2) fault (Figure 4f). In contrast to previous simulations with bounding faults only (B1/B2), near-lithostatic fluid pressures of the ascending magmatic fluids can be maintained in this central fault zone. Hence, also the brine phase can be transported upwards to the magmatic-meteoric interface at shallow depths of 1–2 km in this scenario.

Increasing the permeability of the structures in the uppermost kilometer from $10^{-14}$ to $10^{-12}$ m$^2$ leads to stronger fluid focusing and cooling at shallow levels due to enhanced mixing with meteoric fluids in the shallow part of the hydrothermal system (Figures 4g and 4h). In contrast to the previous simulation (Figure 3f), the two-phase

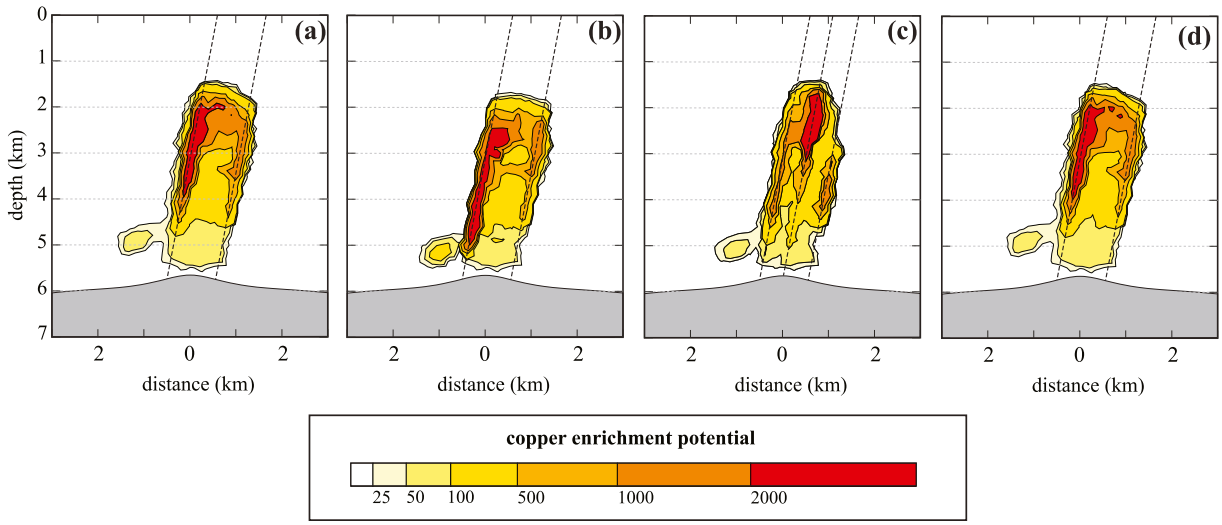


**Figure 5.** Calculated copper enrichment potential of the modeled magmatic-hydrothermal systems after 100,000 years with (a) two subvertical bounding faults (Figure 3), (b) a higher permeability in the left (B1) fault (Figure 4a), (c) three subvertical faults (Figure 4d) and (d) two subvertical faults with higher permeabilities at shallow levels (Figure 4g).

area is less extensive (Figure 4i) because the ascending magmatic fluids (mainly vapor) contract to a single-phase liquid during mixing with meteoric water.

#### 3.2.3. Ore-Formation Potential

The thermal evolution of fluid flow systems controls the varying potential for primary, structurally controlled copper precipitation within the assumed temperature interval of 450°C to 350°C (Figure 5). In the scenario with a permeability of $10^{-14}$ $m^2$ in the two bounding structures, higher-grade copper (>500 enrichment potential) occurs from 2 to 3 km depth, which corresponds to the depth where the temperature-pressure front is maintained during the peak of the hydrothermal system (Figure 5a). The gradual retreat of this front with time leads to the formation of an elongated, cylindrical-shaped copper enrichment zone toward deeper levels along the two structures (ca. 4.5 km depth). However, values for copper potential above 2,000 are limited to the left fault (F1), where most of the cooling occurs due to incoming ambient fluids.

In the scenario with a higher permeability in the left (B1) fault, the general shape of the shell is maintained, and very high grades (>2,000) reach depths up to 5.5 km (Figure 5b), showing that cooling of the ascending magmatic fluid by mixing with ambient fluids occurs along a depth range of 3 km. In the scenario with three fault zones (Figure 5c), the highest copper grades (>2,000) are calculated for the up-flow zone along the central structure, between ~1.8 and 3 km depth (Figure 4f). Additional copper enrichment potentials above 500 also occur along the left (B1) and right (B2) fault zones up to 4.5 km depth (Figure 5c). Finally, the scenario with higher permeabilities in the structures at shallower levels (Figure 5d) is very similar to the first (Figure 5a), showing that the increase in permeability at shallow levels does not affect the copper precipitation potential or the location of the shells.

### 3.3. Subhorizontal Magmatic-Hydrothermal Vein-Type Deposits

#### 3.3.1. Dynamic Structure Permeability

In the initial expulsion phase of the scenario with steeply dipping structures up to the fourth level of horizontal structures, fluids preferentially use the two structures above the magma chamber (V1 and V2; Figure 6a). Fluid release leads to a strong increase in fluid pressures (>100 MPa) and additional porosity after reaching the failure criterion (Figure 6b) in the entire domain above the intrusion with maximum values (1%) along the injection point (FR) followed by the four fractures and the connecting faults (0.1%) which serve as major fluid pathways to accommodate the additional fluid mass. In this simulation, injected magmatic fluids remain in a single-phase state (Figure 6b) with salinities of 5 wt.% NaCl. Fluid flow is characterized by velocities of about

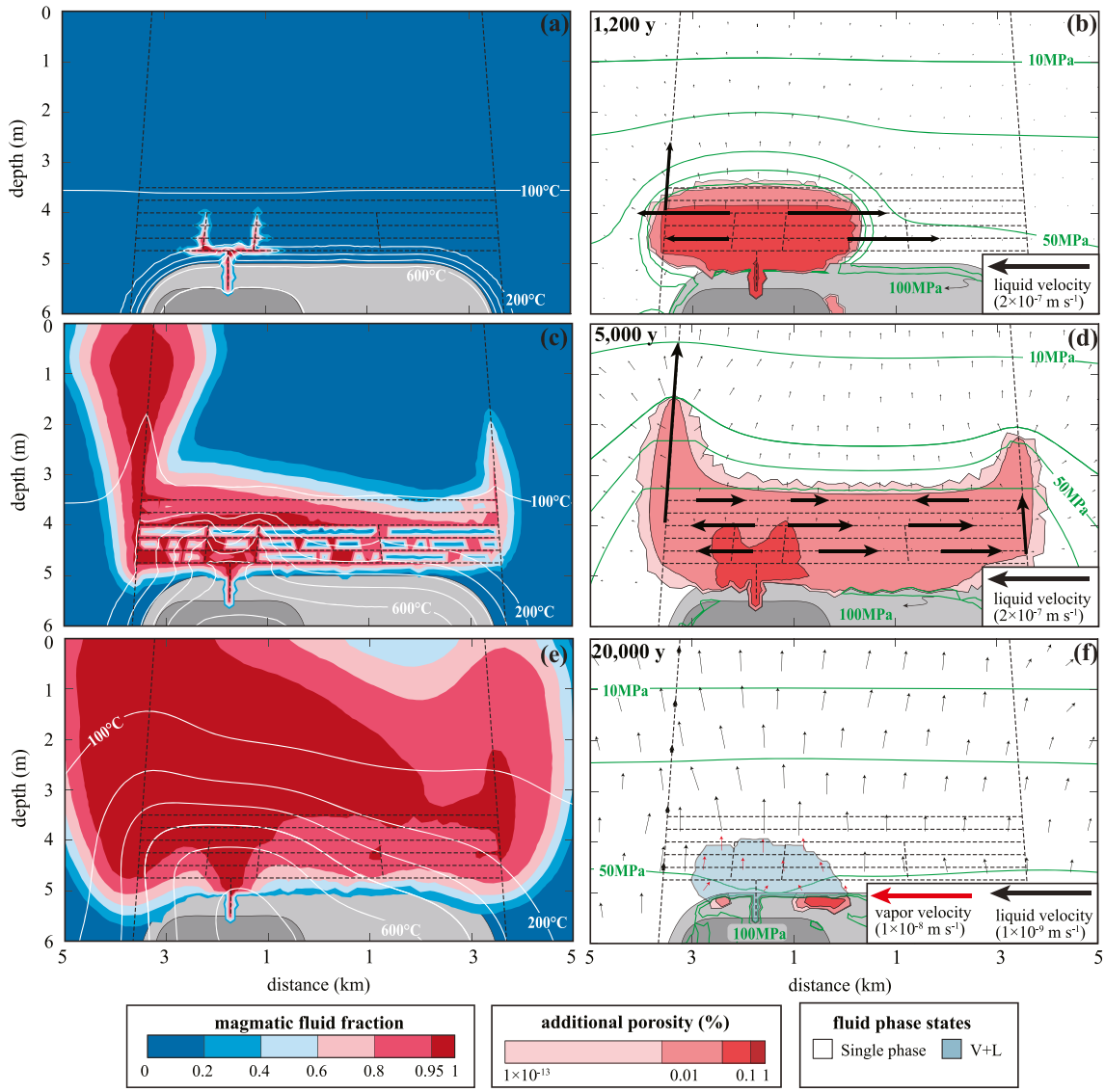


**Figure 6.** Temporal and spatial evolution of a magmatic-hydrothermal system with structurally controlled fluid flow along horizontal structures, connected by three subvertical structures (F1, F2, and F3) up to the fourth level and two subvertical bounding faults with dynamic permeability after 1,200 years (a, b), 5,000 years (c, d) and 20,000 years (e, f), showing: (a, c, e) the fraction of magmatic fluids and the temperature (white lines); (b, d, f) additional porosity, fluid pressure (black lines) as well as fluid phase states (only in f) and liquid (*L*) and vapor (*V*) velocities.

$2 \times 10^{-7}$ m/s along the interconnected fractures and the vertical bounding fault (B1) and negligible velocities in the low-permeability host rocks.

After 5,000 years of simulation time, fluids flow in all fault zones (B1, V1, V2, V3, and B2) (Figure 6c) and enter the uppermost two fractures through the bounding faults (Figure 6d). Magmatic fluids dominate the left-hand side of the modeling domain, but the thermal front is decoupled from the magmatic fluid front. Fluid pressures are still high but significantly lower in comparison with the initial stages (<100 MPa) along the structures (Figure 6d). Consequently, the additional porosity reaches the highest values (0.1%) immediately above the cupola and along the two vertical structures (F1 and F2, Figure 7d).

At the waning stage (20,000 years), the entire domain is still dominated by magmatic fluids. Most fluids have been released from the cooling magma chamber, and only a small fraction is still above the solidus temperature of 650°C. The temperature along the fractures is still considerably high (from 300°C to >600°C). Due to the relaxation of the fluid overpressure, the fluids now reach a two-phase state around the injection location (Figure 6f).

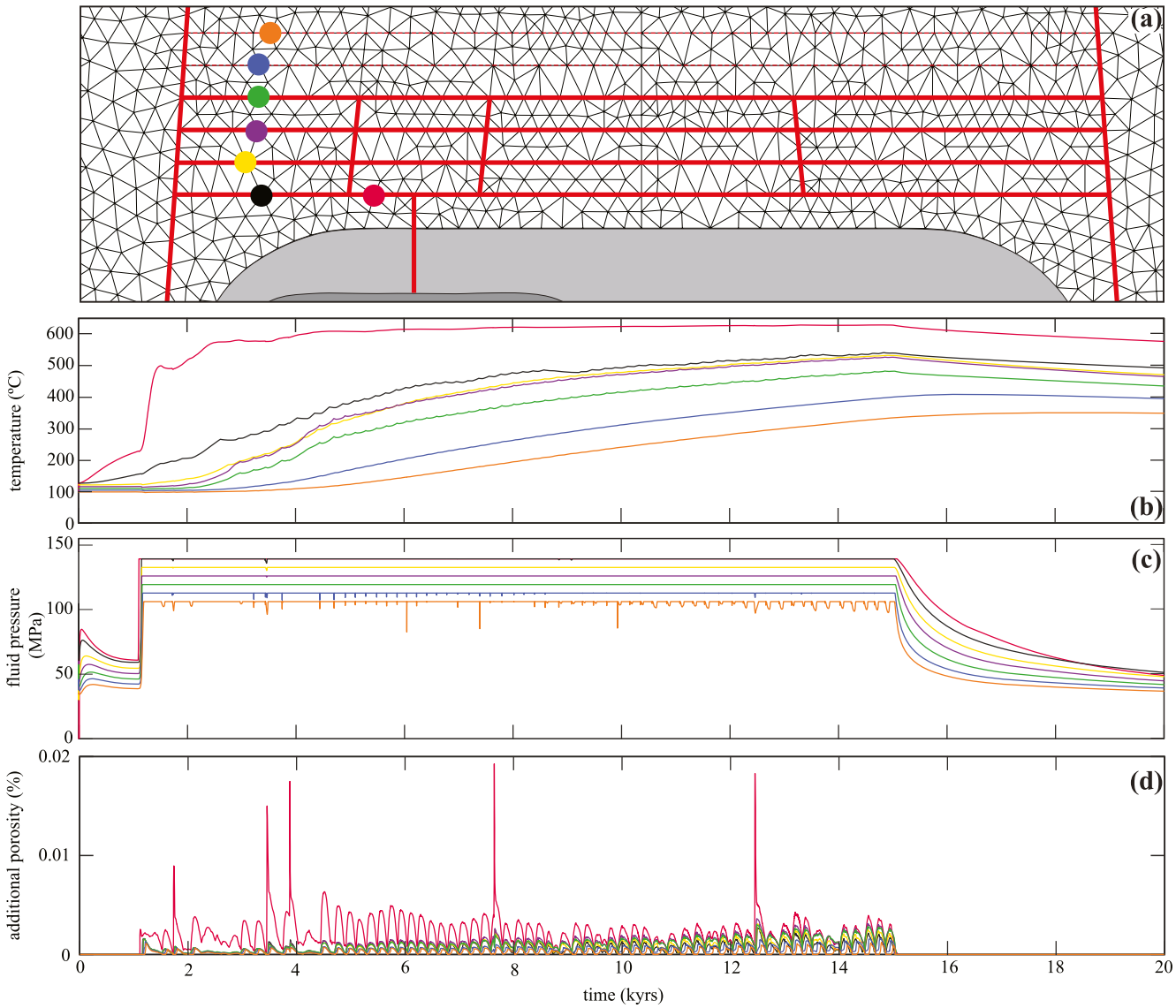


**Figure 7.** Temporal evolution at selected observation points within the horizontal structures (a) of temperature (b), fluid pressure, and (c) additional porosity (d) for the simulation shown in Figure 6.

Fluid flow through the structures has become negligible due to the dynamic closure, and the remaining outward flow is now accommodated by very small velocities through the low-permeability host rock. In contrast to the simulations of the porphyry systems, the incursion of meteoric water is hampered by the low permeability of the host rock and the dynamic closure of the structures at fluid pressures below the failure criterion.

The simulations with dynamic permeability in the structures show a pulsating behavior of the hydrothermal system, as shown by the temporal evolution of temperature, fluid pressure, and additional porosity at selected observation points along the six horizontal structures (Figure 7). The temperature profile (Figure 7b) shows that the temperature right above the magma chamber (red circle in Figure 7a; red line in Figure 7b) rises sharply as soon as the fluids are released (~1,000 years) and stays steady at ca. 600°C for more than 20,000 years. In contrast, the temperature at the other locations indicates that heat transfer is dominated by conduction. Fluid pressure rises immediately to values between ~25 and 75 MPa, relaxes slightly, and at the time of fluid release, it rises to values above 100 MPa, with fluctuations over time, which are coincident with periods of opening and closure of the porosity and permeability (Figure 7d), that is, stages of crack and seal of the fractures.

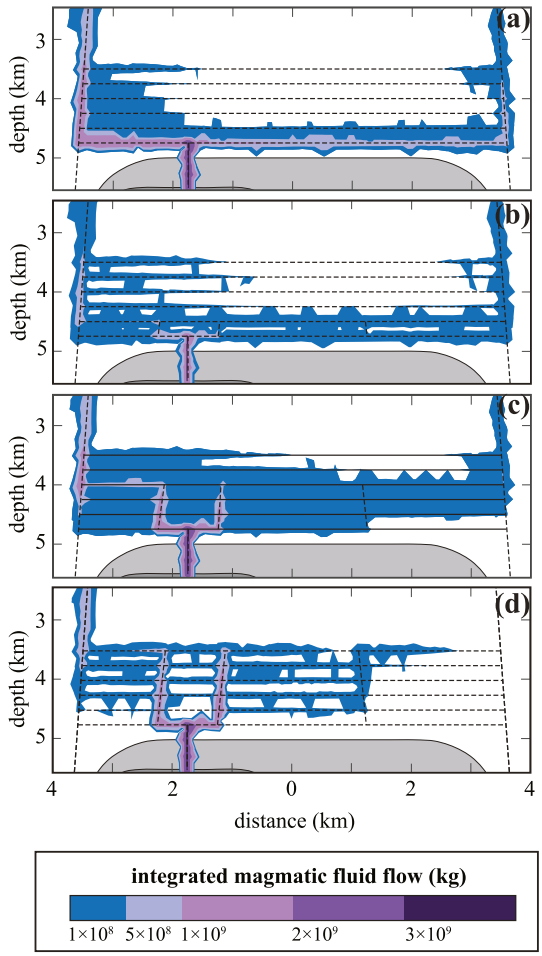


**Figure 8.** Calculated integrated magmatic fluid flow of the modeled magmatic-hydrothermal systems after 100,000 years with two subvertical bounding faults (B1, B2) and connectivity to no (a), two (b) four (c), and all six (d) higher levels of horizontal structures along V1, V2, and V3 with dynamic permeability evolution.

#### 3.3.2. Ore-Formation Potential

Assuming that the magmatic fluids introduce the metals and ore deposition is controlled by fluid-rock interaction, we monitor the preferred pathways for magmatic fluid fluxes in the hydrothermal system by considering different levels of connectivity between the horizontal structures (Figure 8; additional simulations shown in the Supporting Information S1). With no vertical connections, most flow occurs along the lowermost structure and the bounding faults. As a result, the highest ore grades are diverted toward the left-hand side of the fracture and B1, with some disseminated mineralization along the structures indicated in dark blue (Figure 8a). When there is connectivity to the second level of structures, the horizontal flow is distributed across the two lowermost structures (Figure 8b). Connections to the fourth and sixth levels demonstrate that fluid flow strongly prefers vertical connections, leading to an increased mass flux to the respective uppermost level that can be reached by structure connectivity (Figures 8c and 8d). In the latter case, the enhanced interconnectivity leads to a stronger focusing of fluid flux to the left side (Figure 8d).

## 4. Discussion

### 4.1. General Implications

The numerical simulations of porphyry systems with vertical fault control show how permeable fault zones promote and influence the formation of copper ore shells at a stable temperature-pressure front where downflowing ambient fluids cool hot, overpressured magmatic fluids by stronger fluid focusing. This mechanism leads to higher-grade zones within the structures, spanning vertically for about 3 km and forming asymmetric ore bodies depending on the structural permeability. Fault locations play a decisive role in fluid focusing: faults located centrally within the fluid injection location are dominated by overpressured pure magmatic fluids. In contrast, faults situated at the borders of the injection location are characterized by mixtures of meteoric and magmatic fluids at near-hydrostatic pressures. The latter can develop so-called heat pipes with the higher-density brine phase flowing downward and the lower-density vapor phase flowing upward. Faults with an increased permeability near the surface impact pure magmatic vapor transport after phase separation at depth and may lead to the selective transport of metals with a vapor phase that contracts to a liquid phase to shallower levels, possibly forming epithermal deposits.

In magmatic-hydrothermal vein-type deposits, mineralization in horizontal structures requires a lack of vertical fluid pathways above the fluid injection location but a hydraulic connection to more distal vertically oriented permeable fault zones. These mechanisms would infer that the primary orientation of the deposit could be controlled by the location of the nearest major vertical high-permeability structures. Observations from natural systems indicate that fracture-controlled magmatic-hydrothermal systems have a dynamic evolution of the permeability due to repeated cycles of failure and crack-sealing of the fractures (Cox, 2020; Foxford et al., 2000; Ramsay, 1980). Our parameterization of this process self-organizes into a pulsating behavior of the hydrothermal system because permeability and porosity increase if fluid pressure reaches the failure criterion but decrease again if overpressure is relaxed. As a result, in-flow of meteoric fluids cannot occur under overpressured conditions but would require that structures remain permeable after stimulation, and that fluid pressures can drop to near-hydrostatic values.

### 4.2. Comparison With Known Deposits

Despite the simplified geometries with relatively coarse meshes, our modeling results show some similarities with the natural deposits from which the schematic structures in our geometry have been taken. Therefore, we can provide new insight into the influence of fault control on ore formation.

The ore body of the Chuquicamata deposit open pit is currently 1,100 m (Length × Width = 4,500 × 3,000 m), and drilling campaigns suggest the existence of at least more than 900 m of mineable ore below the "final pit bottom" (i.e., below 1,800 m) currently has an estimated vertical extension of 2,700 m (Flores & Catalan, 2019; Olavarría et al., 2006). The highest copper contents (>1.5%) are located between the W and the Americana fault (represented by B1 and F1 in our models). Geologic observations indicate that the W fault zone has been active during the emplacement of the intrusions, the formation of the mineralization, and the post-mineral displacement of the orebodies (Dilles et al., 1997; Tomlinson & Blanco, 1997). The late reactivation of the structure is interpreted to have led to increased permeability and enhanced subsequent supergene activity (Faunes et al., 2005; Ossandon et al., 2001), which is not resolved in our model for hypogene mineralization. However, our simplified model for hypogene ore formation already reproduces similar copper distributions.

The highest temperatures in our modeling results are reached in the up-flow zone between the left (B1) and right (B2) bounding faults, irrespective of whether F1 is a higher-permeability structure or not. At Chuquicamata, this part is dominated by potassic alteration, which likely documents the highest temperatures of the ascending magmatic plume. However, in the absence of a central high-permeability fault, mineralization is predominantly located in the left (B1) fault zone, where fluids from the hot up-flow zone are cooled by the increased fluid flux and admixing of meteoric water, which may therefore indicate that preferred copper enrichment in the left (B1) fault zone could already have dominated the stage of hypogene ore formation. It has been suggested that the orebody represents less than 30% of the entire deposit and that the remaining parts have been displaced by the W-fault system (Faunes et al., 2005) by 7 and 35 km to the South (Zentilli et al., 2021). However, our simulations indicate that high-permeability fault zones can act as hydrological divides and lead to highly asymmetric systems, such as in Figure 4a, where the domain left of the W fault remains almost completely unaffected by the input of magmatic fluids. Hence, it is also possible that the displaced, undiscovered parts at Chuquicamata are significantly less mineralized and altered, or even barren.

The simulation with higher permeabilities in the first kilometer (Figures 4g–4i) further shows how the structural control can lead to the ascent of a pure magmatic vapor after phase separation at depth. In this simulation (Figure 4i), vapor ascends, and brine descends at ca. 2 km. The ascending vapor is then cooled as it mixes with ambient fluids, thereby contracting to a liquid phase (Heinrich et al., 2004). This magmatic vapor phase may selectively transport elements like Au and As from the porphyry environment to shallower levels, where fluid-rock interaction and/or boiling could then lead to Au precipitation, as proposed for the formation of epithermal and Carlin-type Au deposits (Heinrich et al., 2004; Muntean et al., 2011).

For the subhorizontal vein-type deposits, our results indicate that the predominantly horizontal orientation of the Panasqueira deposit with mineralization spanning about 500 m in the vertical and at least 2 km in the horizontal direction (Kelly & Rye, 1979) requires the lack of vertical fluid pathways immediately above the deposit (Figures 6, 7, and 8). Fluids are pushed laterally into pre-existing horizontal structures, interpreted to have been generated by transpressional and/or compressional tectonics (Jacques et al., 2018), toward a vertical high-permeability zone at a further distance, such as the nearby Cebola fault (Thadeu, 1951). These mechanisms would infer that the main orientation of the deposit could be controlled by the location of the nearest major vertical high-permeability structures (Figure 6). In fact, the Cebola fault shows some degree of base metal mineralization (Thadeu, 1951, 1979). However, the respective timing in comparison with the formation of the Panasqueira deposit is unknown.

The simulated permeability evolution in the horizontal structures has to rely on a number of assumptions and, therefore, cannot serve as a quantification of the ore-forming processes. However, we note that the flow velocities obtained with our models have comparable orders of magnitude to those calculated using growth bands from tourmaline at the Panasqueira deposit (Launay et al., 2018), whose values obtained range from $10^{-4}$ to $10^{-3}$ m/s and $10^{-6}$ to $10^{-5}$ m/s for the veins and host rocks, respectively.

Recent geochemical studies at Panasqueira further indicate that the early alteration and mineralization stages occurred at high temperatures of about 500°C (Codeço et al., 2017, 2019; Martins et al., 2020; Mateus et al., 2020). On the other hand, fluid inclusion studies have identified a single-phase magmatic fluid of about 300°C for the main ore stage (Lecumberri-Sanchez et al., 2017), while incursion of meteoric fluids and vapor-brine coexistence only occurs during the late stages (Kelly & Rye, 1979; Lecumberri-Sanchez et al., 2017). Our numerical simulations cannot resolve this discrepancy in temperature estimates because the approach cannot resolve the detailed thermal evolution at the vein-host rock interface but instead assumes that fluid and rock are in thermal equilibrium within a given mesh volume. However, the results provide some insights into the thermal evolution on a scale of several kilometers. The temporal evolution at different levels and distances from the cupola shows that the temperature near the injection location is rapidly controlled by the temperature of the magmatic fluid, almost instantly reaching 600°C (Figure 6). At further distances and with increased divergence of the fluids into several structures, the temperature is increasingly controlled by the host rock, which only gets gradually heated due to conduction from the hot magmatic intrusion and by continuous throughflow of magmatic fluids. Contrary to common assumptions, these parts of the system experience a gradual increase in temperature during the fluid release phase, even though the rate and temperature of fluid release remain more or less the same.

## 5. Conclusions

This study introduces a modified mixed-dimensional element approach to resolve structurally controlled ore formation in magmatic-hydrothermal systems. Our results show that the representation of structures by lower-dimensional elements enables using coarse-resolution meshes to save computational time but still captures the first-order fluid dynamics. We applied this approach to model magmatic-hydrothermal deposits controlled by vertical and horizontal structures.

The simulations show that vertically oriented high-permeability fault zones in porphyry copper systems can lead to increased fluid focusing, resulting in vertically extended high-grade deposits with asymmetric ore shells. Depending on the location of the structures, this focused flow is controlled by overpressured, purely magmatic fluids or by a mixture of magmatic and meteoric fluids at sub-hydrostatic pressures. The latter can lead to the formation of so-called heat pipes, which promote phase separation and the ascent of the magmatic vapor phase into epithermal systems.

The results further indicate that the formation of subhorizontal magmatic-hydrothermal vein-type deposits requires a lack of vertical fluid pathways above the injection location of magmatic fluids. Our results with dynamic permeability in the structures show a pulsating behavior of the ore system with fluid pressure fluctuations causing porosity and permeability increases and decreases, corresponding to crack-seal cycles observed in natural systems. The incursion of meteoric water into the vein system at late stages would only be possible if structure permeability remains at least partially open after stimulation and subsequent pressure relaxation.

Despite the generic character of the geometries and simplified representation of key structures in the modeling domain, the simulations can already reproduce key observations from known deposits, such as the vertically extended Chuquicamata porphyry deposit and the subhorizontally oriented vein system of the Panasqueira deposit. These similarities demonstrate that the permeability and connectivity of geological structures can be critical parameters to generate fluid focusing in magmatic-hydrothermal systems and control the potential to form economic ore deposits.

## Data Availability Statement

The study uses the software CSMP++ and the algebraic multi-grid solver SAMG, which are subject to licensing via https://mineralsystems.ethz.ch/software/csmp.html and https://www.scai.fraunhofer.de/de/geschaeftsfelder/schnelle-loeser/produkte/samg.html. The necessary information on the numerical method and the simulation setups is provided in the methods section and the references therein (Weis, 2015; Weis et al., 2012, 2014).

**Acknowledgments**
We thank the CSMP++ community for many discussions and support. We further thank Stephen Cox and an anonymous reviewer for their insightful reviews, which helped to improve the manuscript. The project was funded by the German Federal Ministry of Education and Research (BMBF) within the project GRAMME (033R149) of the r4 funding initiative. Marta Codeço is further supported by the German Research Foundation (DFG) within the project Melts-Fluids-Models (GL 945/1-1). Additional support has been granted by the Helmholtz Recruitment Initiative awarded to Prof. Dr. Sarah Gleeson. Open Access funding enabled and organized by Projekt DEAL.

## References

Agheshlui, H., Sedaghat, M. H., & Matthai, S. (2018). Stress influence on fracture aperture and permeability of fragmented rocks. *Journal of Geophysical Research: Solid Earth*, *123*(5), 3578–3592. https://doi.org/10.1029/2017JB015365

Andersen, C., Rüpke, L., Hasenclever, J., Grevemeyer, I., & Petersen, S. (2015). Fault geometry and permeability contrast control vent temperatures at the Logatchev 1 hydrothermal field, Mid-Atlantic Ridge. *Geology*, *43*(1), 51–54. https://doi.org/10.1130/G36113.1

Blundy, J., Afanasyev, A., Tattitch, B., Sparks, S., Melnik, O., Utkin, I., & Rust, A. (2021). The economic potential of metalliferous sub-volcanic brines. *Royal Society Open Science*, *8*(6), 202192. https://doi.org/10.1098/rsos.202192

Burnham, C. W. (1979). Magmas and hydrothermal fluids. In H. L. Barnes (Ed.), *Geochemistry of hydrothermal ore deposits* (2nd ed., pp. 71–136). John Wiley and Sons.

Bussink, R. W. (1984). Geochemistry of the Panasqueira tungsten-tin deposit, Portugal. *Geologica Ultraiectina*, *33*, 170.

Černý, P., Blevin, P. L., Cuney, M., & London, D. (2005). Granite-related ore deposits. *Society of Economic Geologist*, *100th Anniversary*, 337–370.

Codeço, M. S., Weis, P., Trumbull, R. B., Glodny, J., Wiedenbeck, M., & Romer, R. L. (2019). Boron isotope muscovite-tourmaline geothermometry indicates fluid cooling during magmatic-hydrothermal W-Sn ore formation. *Economic Geology*, *114*(1), 153–163. https://doi.org/10.5382/econgeo.2019.4625

Codeço, M. S., Weis, P., Trumbull, R. B., Pinto, F., Lecumberri-Sanchez, P., & Wilke, F. D. H. (2017). Chemical and boron isotopic composition of hydrothermal tourmaline from the Panasqueira W-Sn-Cu deposit, Portugal. *Chemical Geology*, *468*(1), 1–16. https://doi.org/10.1016/j.chemgeo.2017.07.011

Codeço, M. S., Weis, P., Trumbull, R. B., van Hinsberg, V., Pinto, F., Lecumberri-Sanchez, P., & Schleicher, A. M. (2021). The imprint of hydrothermal fluids on trace-element contents in white mica and tourmaline from the Panasqueira W–Sn–Cu deposit, Portugal. *Mineralium Deposita*, *56*(3), 481–508. https://doi.org/10.1007/s00126-020-00984-8

Coumou, D., Driesner, T., & Heinrich, C. A. (2008). The structure and dynamics of Mid-Ocean Ridge hydrothermal systems. *Science*, *321*(5897), 1825–1828. https://doi.org/10.1126/science.1159582

Cox, S. F. (2005). Coupling between deformation, fluid pressures, and fluid flow in ore-producing hydrothermal systems at depth in the crust. In J. W. Hedenquist, J. F. H. Thompson, R. J. Goldfarb, & J. P. Richards (Eds.), *One Hundredth Anniversary* (pp. 39–75). Society of Economic Geologists. https://doi.org/10.5382/AV100.04

Cox, S. F. (2020). The dynamics of permeability enhancement and fluid flow in overpressured, fracture-controlled hydrothermal systems. In J. V. Rowland, & D. A. Rhys (Eds.), *Applied structural geology of ore-forming hydrothermal systems* (pp. 25–82). Society of Economic Geologists. https://doi.org/10.5382/rev.21.02

Cox, S. F., Knackstedt, M., & Braun, J. (2001). Principles of structural control on permeability and fluid flow in hydrothermal systems. In *Structural controls on ore genesis* (pp. 1–24). Society of Economic Geologists. https://doi.org/10.5382/Rev.14.01

Dilles, J. H. (1987). Petrology of the Yerington Batholith, Nevada; evidence for evolution of porphyry copper ore fluids. *Economic Geology*, *82*(7), 1750–1789. https://doi.org/10.2113/gsecongeo.82.7.1750

Dilles, J. H., Tomlinson, A. J., Martin, M. W., & Blanco, N. (1997). El Abra and Fortuna complexes: A porhyry copper batholith sinistrally displaced by the Falla Oeste [ext. abs.]. *Congreso Geológico Chileno, 8th, Antofagasta, Chile, Actas, v. 3*.

Driesner, T. (2007). The system $H_2O$-NaCl. Part II: Correlations for molar volume, enthalpy, and isobaric heat capacity from 0 to 1000°C, 1 to 5000 bar, and 0 to 1 XNaCl. *Geochimica et Cosmochimica Acta*, *71*(20), 4902–4919. https://doi.org/10.1016/j.gca.2007.05.026

Driesner, T., & Heinrich, C. A. (2007). The system $H_2O$-NaCl. Part I: Correlation formulae for phase relations in temperature-pressure-composition space from 0 to 1000°C, 0 to 5000 bar, and 0 to 1 XNaCl. *Geochimica et Cosmochimica Acta*, *71*(20), 4880–4901. https://doi.org/10.1016/j.gca.2006.01.033

Faunes, A., Hintze, F., Siña, A., Véliz, H., Vivanco, M., & Staff (of 2003). (2005). Chuquicamata, core of a planetary scale Cu-Mo anomaly. In T. M. Porter (Ed.), *Super porphyry copper & gold deposits: A global perspective* (pp. 151–174). Adelaide PGC Publishing. (PDF here if helpful Retrieved from https://www.researchgate.net/publication/335276774_Chuquicamata_Core_of_a_Planetary_Scale_Cu-Mo_Anomaly)

Flores, G., & Catalan, A. (2019). A transition from a large open pit into a novel "macroblock variant" block caving geometry at Chuquicamata mine, Codelco Chile. *Journal of Rock Mechanics and Geotechnical Engineering*, *11*(3), 549–561. https://doi.org/10.1016/j.jrmge.2018.08.010

Fournier, R. O. (1999). Hydrothermal processes related to movement of fluid from plastic into brittle rock in the magmatic-epithermal environment. *Economic Geology*, *94*(8), 1193–1211. https://doi.org/10.2113/gsecongeo.94.8.1193

Foxford, K. A., Nicholson, R., Polya, D. A., & Hebblethwaite, R. P. B. (2000). Extensional failure and hydraulic valving at Minas da Panasqueira, Portugal: Evidence from vein spatial distributions, displacements and geometries. *Journal of Structural Geology*, *22*(8), 1065–1086. https://doi.org/10.1016/S0191-8141(00)00029-8

Geiger, S., & Emmanuel, S. (2010). Non-Fourier thermal transport in fractured geological media. *Water Resources Research*, *46*(7), 1–13. https://doi.org/10.1029/2009WR008671

Gruen, G., Weis, P., Driesner, T., Heinrich, C. A., & de Ronde, C. E. J. J. (2014). Hydrodynamic modeling of magmatic-hydrothermal activity at submarine arc volcanoes, with implications for ore formation. *Earth and Planetary Science Letters*, *404*, 307–318. https://doi.org/10.1016/j.epsl.2014.07.041

Hasenclever, J., Theissen-Krah, S., Rüpke, L. H., Morgan, J. P., Iyer, K., Petersen, S., & Devey, C. W. (2014). Hybrid shallow on-axis and deep off-axis hydrothermal circulation at fast-spreading ridges. *Nature*, *508*(7497), 508–512. https://doi.org/10.1038/nature13174

Hayba, D. O., & Ingebritsen, S. E. (1997). Multiphase groundwater flow near cooling plutons. *Journal of Geophysical Research*, *102*(B6), 12235–12252. https://doi.org/10.1029/97JB00552

Hedenquist, J. W., & Lowenstern, J. B. (1994). The role of magmas in the formation of hydrothermal ore deposits. *Nature*, *370*(6490), 519–527. https://doi.org/10.1038/370519a0

Heinrich, C. A., & Candela, P. A. (2014). Fluids and ore formation in the Earth's crust. In H. D. Holland & K. K. Turekian (Eds.), *Treatise on Geochemistry, 2nd edition*, (Vol. 13, pp. 1–28). Elsevier. https://doi.org/10.1016/B978-0-08-095975-7.01101-3

Heinrich, C. A., Driesner, T., Stefánsson, A., & Seward, T. M. (2004). Magmatic vapor contraction and the transport of gold from the porphyry environment to epithermal ore deposits. *Geology*, *32*(9), 761. https://doi.org/10.1130/G20629.1

Ingebritsen, S. E., Geiger, S., Hurwitz, S., & Driesner, T. (2010). Numerical simulation of magmatic hydrothermal systems. *Reviews of Geophysics*, *48*(1), RG1002. https://doi.org/10.1029/2009RG000287

Ingebritsen, S. E., & Manning, C. E. (1999). Geological implications of a permeability-depth curve for the continental crust. *Geology*, *27*(12), 1107. https://doi.org/10.1130/0091-7613(1999)027<1107:GIOAPD>2.3.CO;2

Ingebritsen, S. E., & Manning, C. E. (2010). Permeability of the continental crust: Dynamic variations inferred from seismicity and metamorphism. In *Frontiers in geofluids* (pp. 193–205). Wiley-Blackwell. https://doi.org/10.1111/j.1468-8123.2010.00278.x

Ingebritsen, S. E., Sanford, W., & Neuzil, C. (2006). *Groundwater in geologic processes* (2nd ed.). Cambridge University Press.
Jacques, D., Vieira, R., Muchez, P., & Sintubin, M. (2018). Transpressional folding and associated cross-fold jointing controlling the geometry of post-orogenic vein-type W-Sn mineralization: Examples from Minas da Panasqueira, Portugal. *Mineralium Deposita*, *53*(2), 171–194. https://doi.org/10.1007/s00126-017-0728-6
Kelly, W. C., & Rye, R. O. (1979). Geologic, fluid inclusion, and stable isotope studies of the tin-tungsten deposits of Panasqueira, Portugal. *Economic Geology*, *74*(8), 1721–1822. https://doi.org/10.2113/gsecongeo.74.8.1721
Kesler, S. E., & Simon, A. C. (2015). *Mineral resources, economics and the environment*. Cambridge University Press. https://doi.org/10.1017/CBO9781139871426
Kissling, W. M., Ellis, S., McNamara, D. D., & Massiot, C. (2015). Modelling fluid flow through fractured rock: Examples using TVZ geothermal reservoirs. In *37th New Zealand geothermal Workshop*. Taupo: Publisher New Zealand Geothermal Workshop.
Korges, M., Weis, P., Lüders, V., & Laurent, O. (2018). Depressurization and boiling of a single magmatic fluid as a mechanism for tin-tungsten deposit formation. *Geology*, *46*(1), 75–78. https://doi.org/10.1130/G39601.1
Lamy-Chappuis, B., Heinrich, C. A., Driesner, T., & Weis, P. (2020). Mechanisms and patterns of magmatic fluid transport in cooling hydrous intrusions. *Earth and Planetary Science Letters*, *535*, 116111. https://doi.org/10.1016/j.epsl.2020.116111
Launay, G., Sizaret, S., Guillou-Frottier, L., Gloaguen, E., & Pinto, F. (2018). Deciphering fluid flow at the magmatic-hydrothermal transition: A case study from the world-class Panasqueira W–Sn–(Cu) ore deposit (Portugal). *Earth and Planetary Science Letters*, *499*, 1–12. https://doi.org/10.1016/j.epsl.2018.07.012
Lecumberri-Sanchez, P., Vieira, R., Heinrich, C. A., Pinto, F., & Wälle, M. (2017). Fluid-rock interaction is decisive for the formation of tungsten deposits. *Geology*, *45*(7), 579–582. https://doi.org/10.1130/G38974.1
Martins, I., Mateus, A., Figueiras, J., Rodrigues, P., & Pinto, F. (2020). Thermal evolution of the W-Sn(-Cu) Panasqueira ore system (Portugal): Insights from pyrite-pyrrhotite and arsenopyrite geothermometers. *Comunicações Geológicas*, *107*(2), 69–74.
Mateus, A., Figueiras, J., Martins, I., Rodrigues, P., & Pinto, F. (2020). Relative abundance and compositional variation of silicates, Oxides and phosphates in the W-Sn-rich Lodes of the Panasqueira mine (Portugal): Implications for the ore-forming process. *Minerals*, *10*(6), 551. https://doi.org/10.3390/min10060551
Matthäi, S. K., & Belayneh, M. (2004). Fluid flow partitioning between fractures and a permeable rock matrix. *Geophysical Research Letters*, *31*(7), 1–5. https://doi.org/10.1029/2003GL019027
Mavko, G., Mukerji, T., & Dvorkin, J. (2009). *The rock physics Handbook*. Cambridge University Press. https://doi.org/10.1017/CBO9780511626753
Muntean, J. L., Cline, J. S., Simon, A. C., & Longo, A. A. (2011). Magmatic-hydrothermal origin of Nevada's Carlin-type gold deposits. *Nature Geoscience*, *4*(2), 122–127. https://doi.org/10.1038/ngeo1064
Olavarría, S., Adriasola, P., & Karzulovic, A. (2006). Transition from open pit to underground mining at chuquicamata, Antofagasta, Chile. In *International symposium of stability of rock slopes in open pit mining and civil engineering* (pp. 421–434). The South African Insitute of Mining and Metallurgy.
Ossandon, C. G., Freraut, C. R., Gustafson, L. B., Lindsay, D. D., & Zentilli, M. (2001). Geology of the chuquicamata mine: A progress Report. *Economic Geology*, *96*(2), 249–270. https://doi.org/10.2113/gsecongeo.96.2.249
Pichavant, M., & Manning, D. (1984). Petrogenesis of tourmaline granites and topaz granites; the contribution of experimental data. *Physics of the Earth and Planetary Interiors*, *35*(1–3), 31–50. https://doi.org/10.1016/0031-9201(84)90032-3
Pinget, M., Dold, B., Zentilli, M., & Fontbote, L. (2015). Reported supergene sphalerite rims at the Chuquicamata porphyry deposit (northern Chile) revisited: Evidence for a hypogene origin. *Economic Geology*, *110*(1), 253–262. https://doi.org/10.2113/econgeo.110.1.253
Pinget, M.-C. (2016). *Supergene enrichment and exotic mineralization at Chuquicamata, Chile (Ph.D. thesis)*. Univ. Genève. https://doi.org/10.13097/archive-ouverte/unige:91513
Polya, D. A. (1988). Efficiency of hydrothermal ore formation and the Panasqueira W–Cu(Ag)–Sn vein deposit. *Nature*, *333*(6176), 838–841. https://doi.org/10.1038/333838a0
Polya, D. A., Foxford, K. A., Stuart, F., Boyce, A., & Fallick, A. E. (2000). Evolution and paragenetic context of low δD hydrothermal fluids from the Panasqueira W-Sn deposit, Portugal: New evidence from microthermometric, stable isotope, noble gas and halogen analyses of primary fluid inclusions. *Geochimica et Cosmochimica Acta*, *64*(19), 3357–3371. https://doi.org/10.1016/S0016-7037(00)00459-2
Ramsay, J. G. (1980). The crack–seal mechanism of rock deformation. *Nature*, *284*(5752), 135–139. https://doi.org/10.1038/284135a0
Ribeiro, R. (2017). *Gravimetric Modelling and geological interpretation of Argemela-Panasqueira area*. Porto University. Retrieved from https://repositorio-aberto.up.pt/handle/10216/110622
Richards, J. P. (2021). Porphyry copper deposit formation in arcs: What are the odds? *Geosphere*, *18*(1), 130–155. https://doi.org/10.1130/GES02086.1
Runyon, S. E., Steele-MacInnis, M., Seedorff, E., Lecumberri-Sanchez, P., & Mazdab, F. K. (2017). Coarse muscovite veins and alteration deep in the Yerington batholith, Nevada: Insights into fluid exsolution in the roots of porphyry copper systems. *Mineralium Deposita*, *52*(4), 463–470. https://doi.org/10.1007/s00126-017-0720-1
Shinohara, H., & Hedenquist, J. W. (1997). Constraints on magma degassing beneath the far southeast porphyry Cu-Au deposit, Philippines. *Journal of Petrology*, *38*(12), 1741–1752. https://doi.org/10.1093/petroj/38.12.1741
Sibson, R. H. (1996). Structural permeability of fluid-driven fault-fracture meshes. *Journal of Structural Geology*, *18*(8), 1031–1042. https://doi.org/10.1016/0191-8141(96)00032-6
Sillitoe, R. H. (2010). Porphyry copper systems. *Economic Geology*, *105*(1), 3–41. https://doi.org/10.2113/gsecongeo.105.1.3
Skarmeta, J. (2021). Structural controls on alteration stages at the chuquicamata copper-molybdenum deposit, Northern Chile. *Economic Geology*, *116*(1), 1–28. https://doi.org/10.5382/ECONGEO.4769
Thadeu, D. (1951). Geologia e jazigos de chumbo e zinco da Beira Baixa. *Boletim Sociedade Geológica de Portugal*, *9*, 1–144.
Thadeu, D. (1979). Le gisement stanno-wolframifère de Panasqueira (Portugal). *Chronique de la Recherche Miniere*, *450*, 35–42.
Tomlinson, A. J., & Blanco, N. (1997). Structural evolution and displacement history of the West fault system, Precordillera, Chile: Part 1. Premineral, history. Part 2. Synmineral, history. In *Congreso Geológico Chileno, VIII, (pp. 1873–1882). Antofagasta: Congreso Geológico Chileno*.
Webster, J., Thomas, R., Foerster, H.-J., Seltmann, R., & Tappen, C. (2004). Geochemical evolution of halogen-enriched granite magmas and mineralizing fluids of the Zinnwald tin-tungsten mining district, Erzgebirge, Germany. *Mineralium Deposita*, *39*(4), 452–472. https://doi.org/10.1007/s00126-004-0423-2
Weis, P. (2015). The dynamic interplay between saline fluid flow and rock permeability in magmatic-hydrothermal systems. *Geofluids*, *15*(1–2), 350–371. https://doi.org/10.1111/gfl.12100
Weis, P., Driesner, T., Coumou, D., & Geiger, S. (2014). Hydrothermal, multiphase convection of $H_2O$-NaCl fluids from ambient to magmatic temperatures: A new numerical scheme and benchmarks for code comparison. *Geofluids*, *14*(3), 347–371. https://doi.org/10.1111/gfl.12080

Weis, P., Driesner, T., & Heinrich, C. A. (2012). Porphyry-copper ore shells form at stable pressure-temperature fronts within dynamic fluid plumes. *Science*, *338*(6114), 1613–1616. https://doi.org/10.1126/science.1225009

Zentilli, M., Graves, M. C., Mathur, R., Hanley, J. J., Heaman, L. M., & Boric, R. (2021). Locating the "Missing half" of the giant Chuquicamata porphyry copper deposit, Chile. In A. Sholeh & R. Wang (Eds.), *Special Publication No. 24*. Society of Economic Geologists. https://doi.org/10.5382/SP.24.05

## Erratum

In the original published version of this article, a red line and "F2" notation incorrectly appeared in Fig. 1(g) as a result of a technical error. The figure has now been replaced with the corrected image, and the revised article may be considered the authoritative version of record.